Crystal transformation of 2D tungstic acid H_2WO_4 to WO_3 for enhanced photocatalytic water oxidation

Jun Ke,[1,2] Hongru Zhou,[1] Jie Liu,[2,3] Xiaoguang Duan,[2] Huayang Zhang,[2] Shaomin Liu,[2] and Shaobin Wang[2]*

[1]School of Chemistry and Environmental Engineering, Wuhan Institution of Technology, Wuhan, 430205, China.

[2]Department of Chemical Engineering, Curtin University, GPO Box U1987, Perth, WA 6845, Australia.

[3]School of Environmental Science and Engineering, North China Electric Power University, Baoding 071003, China.

*Correspondence author: Email: shaobin.wang@curtin.edu.au

Abstract

New photocatalytic materials for stable reduction and/or oxidization of water by harvesting a wider range of visible light are indispensable to achieve high practical efficiency in artificial photosynthesis. In this work, we prepared 2D $WO_3 \cdot H_2O$ and WO_3 nanosheets by an one-pot hydrothermal method and sequent calcination, focusing on the effects of crystal transformation on band structure and photocatalytic performance for photocatalytic water oxidation in the presence of electron acceptors (Ag^+) under simulated solar light irradiation. The as-prepared WO_3 nanosheets exhibit enhanced rate of photocatalytic water oxidation, which is 6.3 and 3.6 times higher than that of $WO_3 \cdot H_2O$ nanosheets and commercial WO_3, respectively. It is demonstrated that the releasing of water molecules in the crystal phase of tungstic acid results in transformation of the crystal phase from orthorhombic $WO_3 \cdot H_2O$ to monoclinic WO_3, significantly improving the activity of photocatalytic water oxidation in the presence of Ag^+ because the shift-up of conduction band of WO_3 matches well with the electrode potential of $Ag^+/Ag(s)$, leading to efficient separation of photoinduced electrons and holes in pure WO_3 nanosheets.

Key words: Photocatalytic water oxidation; 2D materials; Crystal transformation; WO_3

Introduction

Photocatalytic production of hydrogen and oxygen by water splitting is one of the most promising but challenging technologies in solving energy demand and environment issues because of its great potential in converting solar energy to chemical energy [1-4]. Nowadays, titanium oxide (TiO_2) as a semiconductor photocatalyst has been still investigated due to its advantages, such as chemical stability, low-cost, and mature fabrication technology [5]. However, TiO_2 is a semiconductor with a wide band gap, only adsorbing UV light, and has a severe issue of recombination of photoinduced electrons and holes, which limits its performance in photo-splitting of water. Alternative semiconductors with intrinsic narrower bandgaps are being explored, such as MoS_2 [6], CdS [7], NiO [8], Co_3O_4 [9], In_2O_3 [10], Fe_2O_3 [11, 12], and Bi_2O_3 [13]. By analyzing the overall water splitting reaction, it is deduced that efficient large-scale production of hydrogen is hindered by the oxygen evolution reaction (OER) due to high energy demand for formation of O=O bond from two water molecules [14]. Therefore, it is generally considered that the valence band (VB) level of a semiconductor should be more positive than the standard redox potential of H_2O/O_2 (1.23 V vs. NHE at pH0; NHE = normal hydrogen electrode) to allow for efficient consumption of photogenerated holes and subsequent production of dioxygen.

Tungsten trioxide (WO_3), known as a nontoxic and photostable *n*-type semiconductor with a band gap of 2.6~2.8 eV, can absorb visible light (< 470 nm) and, therefore, it becomes a compelling photocatalyst for solar light harvesting [15-17]. In general, owing to insufficient conduction band level for photo-splitting of water reaction, WO_3 is unable to reduce water to hydrogen, while it shows a very high activity for water oxidation to oxygen in the presence of a suitable electron acceptor, such as IO_3^-/I^- or Fe^{3+}/Fe^{2+} in water splitting systems [18,19]. Recently, Suzuki et al. reported that tungstic acid monohydrate (H_2WO_4 or $WO_3 \cdot H_2O$) could function as an efficient and stable O_2-evolving photocatalyst with an Fe^{3+}/Fe^{2+} electron scavenger by harvesting visible light up to 500 nm under acidic condition, which is beyond the absorption edge of WO_3 [20]. On the other hand, $WO_3 \cdot H_2O$

was usually used as a precursor to fabricate WO_3 in the past due to the different priorities in the growth process [21]. However, the detailed physicochemical properties and photocatalytic performance of $WO_3 \cdot H_2O$ have rarely been investigated. Particularly, the relationship between crystal phase transformation and photocatalytic water oxidation of $WO_3 \cdot H_2O$ to WO_3 has not been reported.

In this work, we prepared 2D $WO_3 \cdot H_2O$ and WO_3 nanosheets by using an one-pot hydrothermal method and sequent calcination, focusing on their crystal transformation, band structures, and photocatalytic performance for photocatalytic water oxidation in the presence of electron acceptors (Ag^+) under simulated solar light irradiation along with their adsorption properties. The effects of crystal transformation of $WO_3 \cdot H_2O$ on physicochemical properties and photocatalytic performance were discussed.

Experimental section

Preparation of $WO_3 \cdot H_2O$ and WO_3 nanosheets

2D $WO_3 \cdot H_2O$ nanosheets were prepared by a facile hydrothermal route. In a typical procedure, 6.12 mmol of $Na_2WO_4 \cdot 2H_2O$ and 1.224 mmol of NH_4F were dissolved into 12.5 mL of purified water and then 12.5 mL of HCl (2 M) was slowly added into the above solution drop by drop. In addition, 1.53 mmol of oxalic acid was dissolved into 25 mL of purified water. The above two solutions were mixed and stirred for 30 min. The mixture was transferred into a 60 mL Teflon autoclave, which was heated to 90 ^oC and maintained at the temperature for 3 h. A pale-yellow sample was collected and dried at 60 ^oC overnight to obtain $WO_3 \cdot H_2O$ nanosheets. Finally, the $WO_3 \cdot H_2O$ nanosheets were calcined at 500 ^oC for 1 h for removing the crystalline water to gain WO_3 nanosheets.

Characterizations

Crystalline phase of the synthesized samples was measured by X-ray diffraction (XRD) using a Rigaku D/max25 system operated at 40 kV and 40 mA with Cu-Kα radiation ($\lambda = 1.5418$ Å) at a scan rate of $5^o \cdot min^{-1}$. Fourier transform infrared spectra (FTIR) were recorded on a Bruker instrument with an ATR correction mode. Thermal analysis (TGA/DTA) measurement of the prepared NPs was done

using Shimadzu (model 60H) and DSC using Shimadzu (model 60). Scanning electron microscopy (SEM) was performed on a JEOL JSM-6360LV field emission microscope at an accelerating voltage of 15 kV. Transmission electron microscopy (TEM) images were taken on a JEOL 2010F. Raman spectra of the samples were recorded by ISA dispersive Raman spectroscopy using an argon ion laser with 633 nm excitation. Diffuse reflectance spectra (DRS) were measured with a Cary 4000 UV-vis spectrometer equipped with an integrating sphere accessory. The Brunauer-Emmett-Teller (BET) analysis was done using a Quantachrome Autosorb Automated Gas Sorption System.

Photocatalytic activity evaluation

The photocatalytic activity of these obtained samples in photocatalytic water oxidation reaction was conducted in a black jacket reactor by using a 300 W Xenon lamp as the simulated solar light. $AgNO_3$ as an electron scavenger was introduced to promote efficient utilization of photoinduced holes in the samples to oxidize water molecules. In a typical procedure, 0.05 g of powder catalysts were added into 200 mL of solution including $AgNO_3$ (0.03 M) and La_2O_3 (0.2 g), an adjustor of pH value in solution. Before the simulated solar light irradiation, the suspension was mixed under vigorous stirring for 30 min. At the same time, the reactor was degassed for removal of O_2. When a O_2 probe presents the dioxygen concentration at zero, the lamp was lightened to trigger water oxidation reaction. Simultaneously, the O_2 concentrations in the reactor were *in situ* measured by using a NEOFOX O_2 probe and recorded in a computer through the software. Furthermore, the as-prepared samples were evaluated in photocatalytic degradation of methylene blue (MB). The concentrations of MB and a catalyst were at 10 mg/L and 0.5 g/L, respectively, and a high-pressure Xe-lamp (300 W, Philips) was used as a simulated solar source. Prior to the illumination, the MB solution was mixed with the catalysts and sonicated for 30 min in dark to establish the adsorption-desorption equilibrium. During the photocatalytic process, 2 mL of the reaction solution was extracted for every 15 min and centrifugated to gain supernatant that was analyzed by a UV-vis spectrophotometer (JASCOV-670). Relevant active species were investigated by adding a quantity of different scavengers in a manner similar to the above MB photodegradation experiment prior to the addition of the catalyst.

Results and Discussion

Structure, composition, and morphology of $WO_3 \cdot H_2O$ and WO_3 nanosheets

The crystal phase structures of the as-prepared samples were characterized by X-ray diffraction patterns (XRD). In Fig. 1, the main diffraction pattern of $WO_3 \cdot H_2O$ nanosheets is consistent with the standard card (JCPDS No. 43-0679), where the peaks at 16.5°, 25.6°, and 35.0° are observed and attributed to the (020), (111), and (131) crystal planes of orthorhombic $WO_3 \cdot H_2O$, respectively [22,23]. After calcination at 500 °C, hydrate water in $WO_3 \cdot H_2O$ was removed, resulting in formation of highly crystalline WO_3 nanosheets. It is found that the prepared WO_3 nanosheets possess strong peaks at 23.1°, 23.6°, and 24.4°, which are ascribed to the characteristic (002), (020), and (200) crystal planes of monoclinic WO_3 (JCPDS No. 43-1035), respectively [24]. This result indicates that tungsten oxide hydrate ($WO_3 \cdot H_2O$) was completely transformed to monoclinic tungsten trioxide after calcination under elevated temperature.

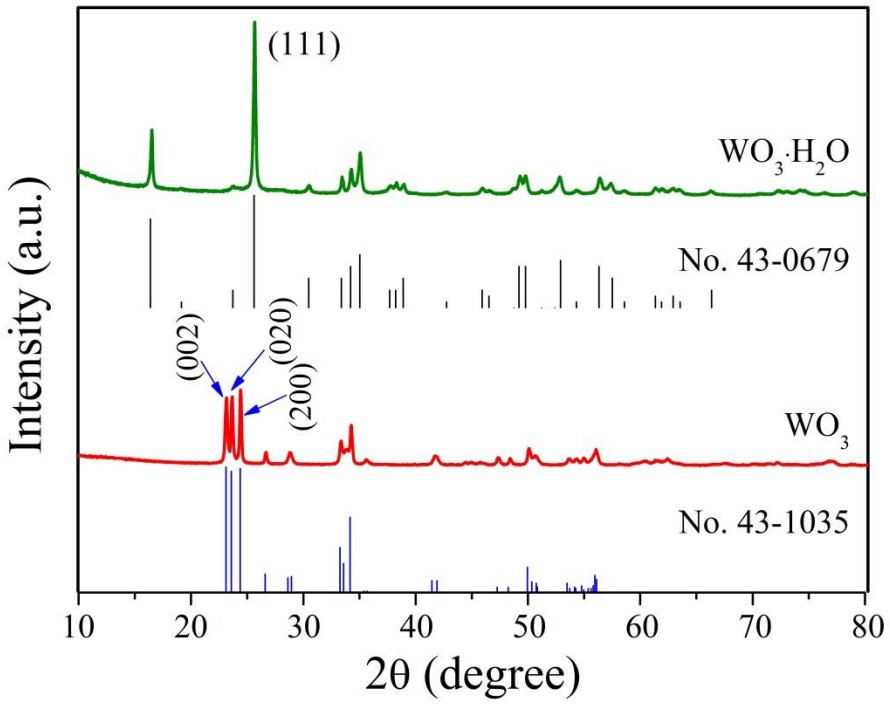

Fig. 1 XRD patterns of the as-obtained $WO_3 \cdot H_2O$ and WO_3 nanosheets.

The morphologies of the as-obtained $WO_3 \cdot H_2O$ and WO_3 samples were analyzed by scanning electron microscopy (SEM, Fig. 2). It is observed that $WO_3 \cdot H_2O$ mainly displays uniform nanosheets

with 350 nm in length and 30 nm in thickness as shown in Fig. 2a and b. Regarding WO_3 nanosheets (Fig. 2c and d), their nanosheet frame was kept but the size of the nanosheet changed apparently after the calcination. The length of the nanosheet shrunk from 350 to 200 nm and the thickness changed from 30 to 20 nm due to releasing of crystalline water in $WO_3 \cdot H_2O$ sample. The formation of 2D nanosheet indicates that the obtained samples possess special crystal facet, which is in a good agreement with the XRD patterns. Meanwhile, SEM images of the WO_3 sample prepared in the absence of oxalic acid show irregular particles (Fig. S1), which testifies the important role of oxalic acid in formation of $WO_3 \bullet H_2O$ nanosheets. By means of adding oxalic acid into the precursor solution, the growth direction of $WO_3 \bullet H_2O$ crystals could be controlled due to the interlayer water in the $WO_3 \bullet H_2O$ snatched by $C_2O_4^{2-}$ ions, resulting in limiting growth of certain crystal facets [25, 26]. Although the interlayer water and oxalic acid were removed owing to the annealing at 500 ^{0}C, resulting in the aggregation of nanosheets (Fig. 2d), the morphology frame of $WO_3 \bullet H_2O$ nanosheets was basically retained, leading to the formation of WO_3 nanosheets.

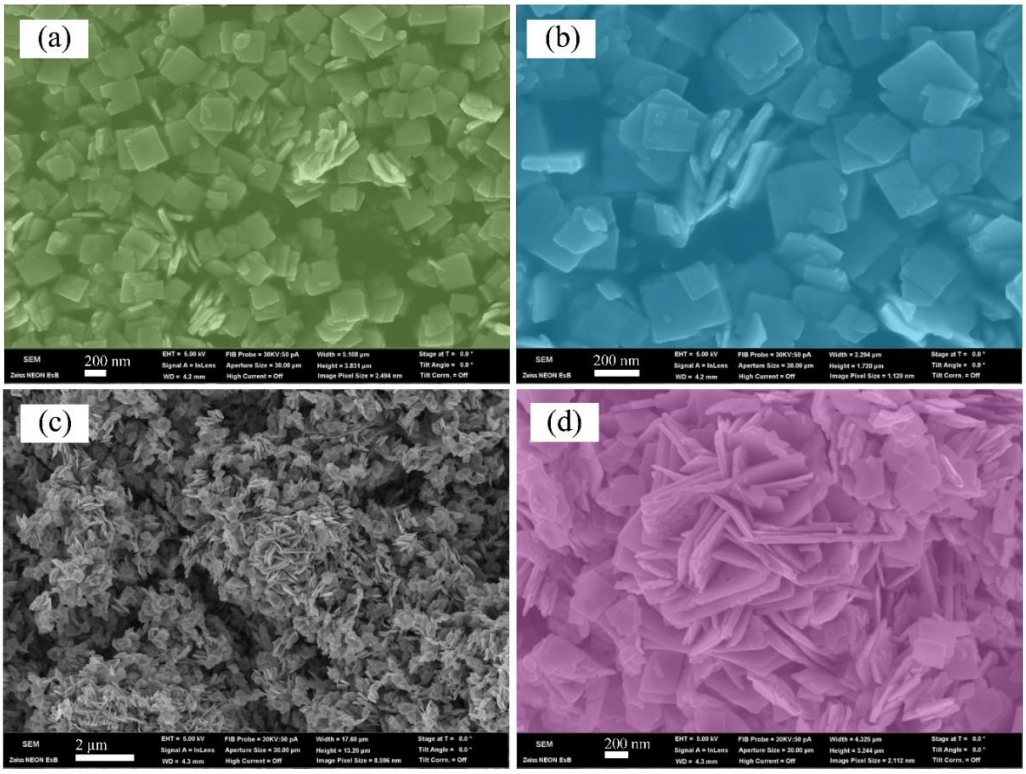

Fig. 2 SEM images of the as-obtained $WO_3 \cdot H_2O$ (a, b) and calcined WO_3 (c, d).

Moreover, HRTEM image of the WO_3 sample is presented in Fig. 3, where 0.387 nm of the lattice fringe on the top/bottom of the nanosheets is ascribed to the (002) facet of monoclinic WO_3 crystals, demonstrating the high exposure of the (002) facet [27, 28]. Meanwhile, the (020) and (002) facets present the similar intensity as the (002) facet in the XRD pattern of WO_3 sample, which indicates that they are exposed at the same time.

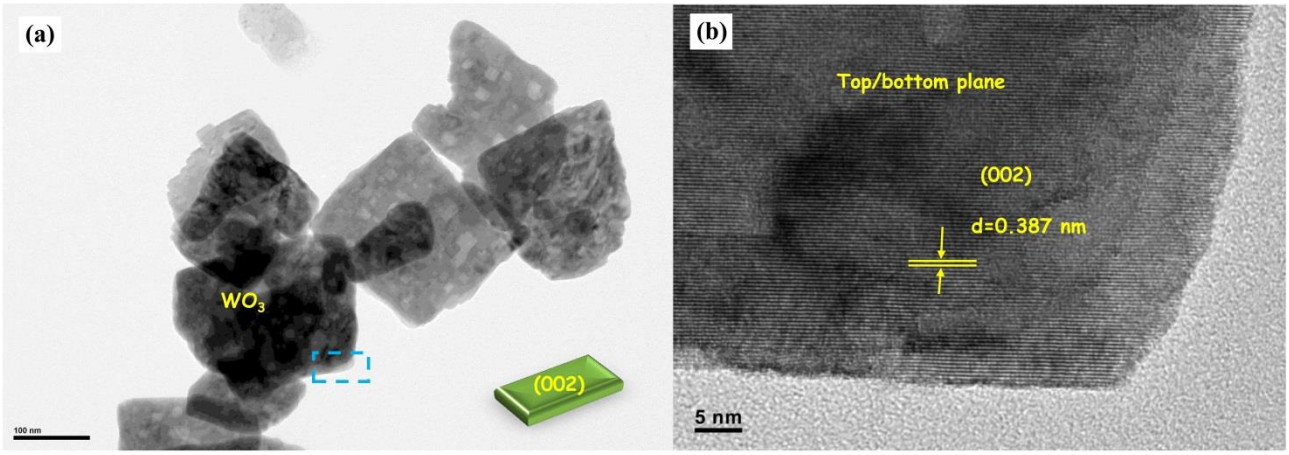

Fig. 3 TEM (a) and HRTEM (b) images of the prepared WO_3 nanosheets.

To further investigate the loss of crystalline water in $WO_3 \cdot H_2O$ sample, thermal gravimetric analysis (TGA) was used to observe the relationship between weigh loss and temperature [29]. The derived TGA curve (red line), as illustrated in Fig. 4a, displayed a principal weight change between 160 and 340 °C, corresponded to the loss of the crystalline water in $WO_3 \cdot H_2O$ [30]. The weight of crystalline water was estimated to be 7.7% in $WO_3 \cdot H_2O$ sample, which demonstrates the molar ratio of WO_3 to H_2O at stoichiometric 1:1. During the calciniation process, the crystalline water was released from $WO_3 \cdot H_2O$, which results in the changes of $WO_3 \cdot H_2O$ crystal structure, as depicted in Fig. 4b. It is seen that the water existing at the interlayer of $WO_3 \cdot H_2O$ disappears, leading to compact bonding between the WO_6 layers, which is the motivation of ultrathin WO_3 nanosheets by intercalation route [31].

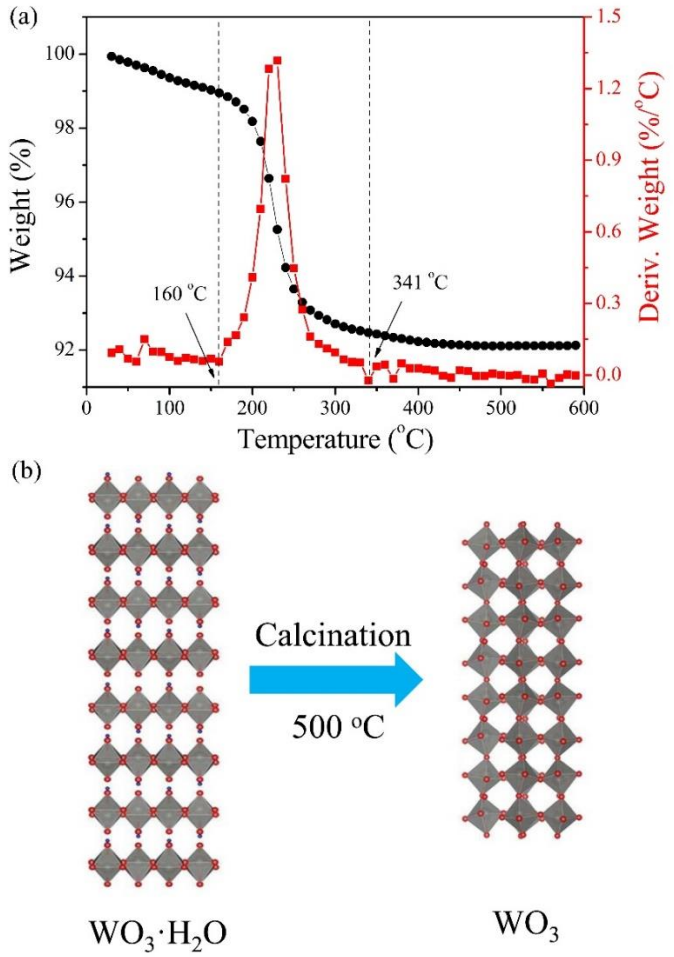

Fig. 4 Thermal gravimetric analysis of the as-prepared $WO_3 \cdot H_2O$ sample.

Raman, FTIR, and optical properties.

As shown in Fig. 5, the surface properties of $WO_3 \cdot H_2O$ and WO_3 nanosheets were verified by FTIR. In the 3600~ 3400 cm^{-1} spectral range, an obvious vibration peak at 3552 cm^{-1} appears due to the stretching vibration of υ(O-H) in $WO_3 \cdot H_2O$ samples, while it disappears in WO_3 sample due to the removal of water at elevated temperature calcination. Meanwhile, the peak at 1673 cm^{-1} in $WO_3 \cdot H_2O$ sample is observed, ascribed to the bending vibration [δ(O-H)] of crystalline water [22, 32]. The WO_6 vibrations within a tunnel-structured framework result in typical absorptions in the spectral region of 1000-400 cm^{-1}, which can be understood by the similar vibrational features in monoclinic WO_3 nanosheets [29]. The sharp shoulder absorption peak at about 965 cm^{-1} is attributed to W=O stretching vibrations, which is also found in $WO_3 \cdot H_2O$ sample. On the other hand, the strong absorption peak at 653 cm^{-1} in $WO_3 \cdot H_2O$ sample is attributed to the υ(O-W-O), which shifted to low frequency 792

cm^{-1} in WO_3 sample. Furthermore, the small absorption at 478 cm^{-1} can be ascribed to υ(O-W-O) bending vibrations in WO_3 nanosheets [33,34]. In the previous reports, the vibration intensity of W=O bands are weaker than that of O-W-O bands due to a large percentage of O-W-O in the bulk WO_3 [35]. In WO_3 nanosheets, the WO_3 grew along the [002] direction, resulting in the increase of W=O percentage.

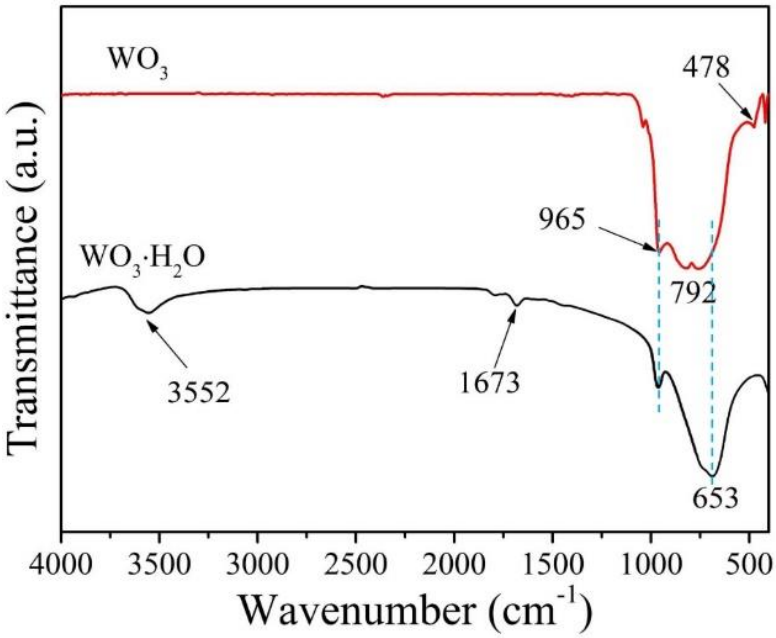

Fig. 5 FTIR spectrum of the $WO_3 \cdot H_2O$ and WO_3 nanosheets.

Raman scattering spectra also confirm the formation of WO_3 nanosheets, displaying two strongest peaks at 715 and 807 cm^{-1} assigned to the stretching vibration of tungsten atom with neighboring oxygen atoms [υ(O-W-O)] (Fig. 6). In addition, two obvious peaks at around 273 and 327 cm^{-1} account for the bending vibration [δ(O-W-O)] [36,37]. Nevertheless, by compared with the Raman spectrum of WO_3, it is found that the corresponding characteristic peaks of W-O and W=O bonds in WO_3 sample are absent in the Raman spectrum of $WO_3 \cdot H_2O$, while two strong peaks at 647 and 944 cm^{-1} are present, which might be ascribed to the characteristic stretching vibrations of W^{6+}-O and terminal W^{6+}-O in orthorhombic $WO_3 \cdot H_2O$ [38, 39]. Furthermore, WO_3 nanosheets were probed by X-ray photoelectron spectroscopy (XPS). In Fig. S2, elements of W 4f and O 1s in WO_3 nanosheets are displayed, calibrated using C 1s (BE = 284.6 eV) as a reference. The high resolution XPS spectrum of W 4f reveals two obvious peaks at 38.1 and 35.9 eV corresponding to W $4f_{5/2}$ and

W $4f_{7/2}$, respectively, which evidently demonstrates the valence state of tungsten element at +6 in the sample of WO_3 [40]. Moreover, there are two apparent binding energy peaks at 531.2 and 528.9 eV in the high resolution XPS spectrum of O 1s, ascribed to the surface adsorbed oxygen species (oxygen vacancy, hydroxyl-like group or the chemisorbed water) and the lattice oxygen species, respectively [41].

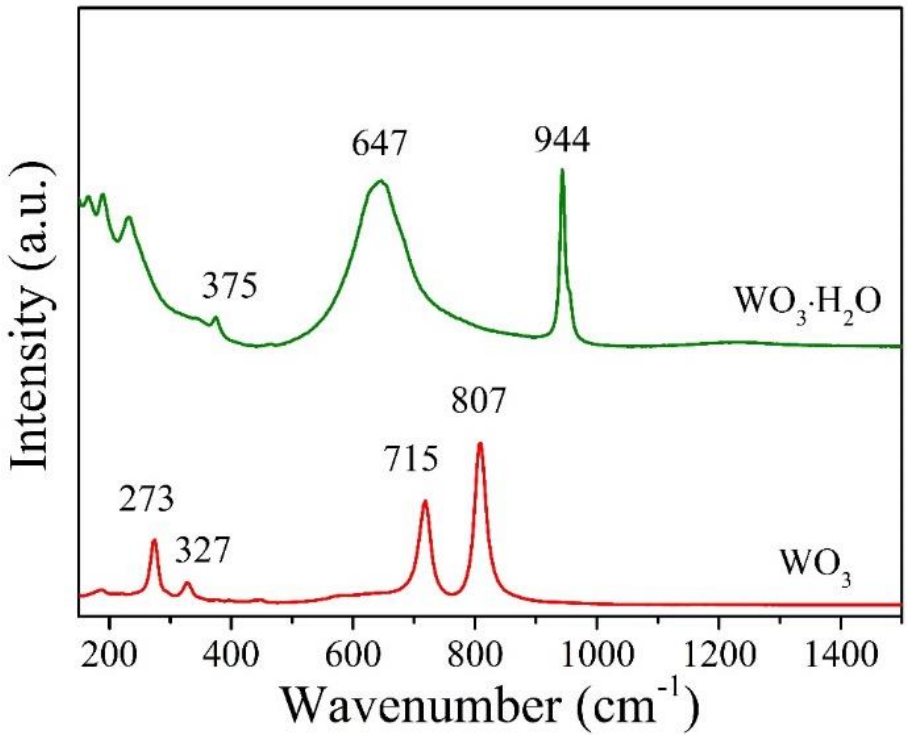

Fig. 6 Raman spectra of the as-prepared $WO_3 \cdot H_2O$ and WO_3 nanosheets.

The optical absorption of the as-prepared $WO_3 \cdot H_2O$ and WO_3 nanosheets was measured, as shown in Fig. 7a. It is found that both the samples have photo respone ranging from UV to visible light and the absorption-edge of $WO_3 \cdot H_2O$ and WO_3 nanosheets are at about 530 and 472 nm, respectively, which implies that the visibl light absorption of $WO_3 \cdot H_2O$ is stronger than WO_3 nanosheets. The optical band gap energies of the as-prepared $WO_3 \cdot H_2O$ and WO_3 samples were calculated from the absorption data by the following equation near the band edge: $\alpha h\nu = A(h\nu - E_g)^{n/2}$, where α, E_g, and A are absorption coefficient, band gap and a constant, respectively. The value of n is 1 or 4 for direct or indirect transition corresponding to $WO_3 \cdot H_2O$ and WO_3, respectively [42, 43]. The values estimated from the interception of the plots are 2.44 and 2.64 eV, as displayed in Fig. 7b. In compared to the

bulk WO_3 (2.60 eV), the as-obtained WO_3 nanosheets present an enlarged band gap, which is originated from the significant quantum confinement effect. Moreover, it is also observed that $WO_3 \cdot H_2O$ nanosheets have a narrower band gap than WO_3 nanosheets, implying $WO_3 \cdot H_2O$ nanosheets could produce more photoinduced charge carriers than that of WO_3 nanosheets. Based on the above results, the conduction band and valence band positions of the prepared samples can be calculated by the following equation: $E_{CB}=X-E^e-0.5E_g$, where X is the Mulliken's electronegativity of the samples, E^e is the energy of a free electron on the hydrogen scale (4.50 eV), and E_g is the bandgap [44, 45]. The values of Mulliken's electronegativity for WO_3 and $WO_3 \cdot H_2O$ are equal to 6.59 and 6.88 eV, respectively. Accordingly, the bottoms of conduction band (CB) of WO_3 and $WO_3 \cdot H_2O$ were calculated to be 0.77 and 1.16 eV, respectively. Consequently, the valence band values (VB) of WO_3 and $WO_3 \cdot H_2O$ were estimated to be 3.41 and 3.60 eV *vs.* NHE, pH0, respectively. It is indicated that both WO_3 and $WO_3 \cdot H_2O$ nanosheets could theoretically oxidize water to evolve O_2 under sunlight irradiation.

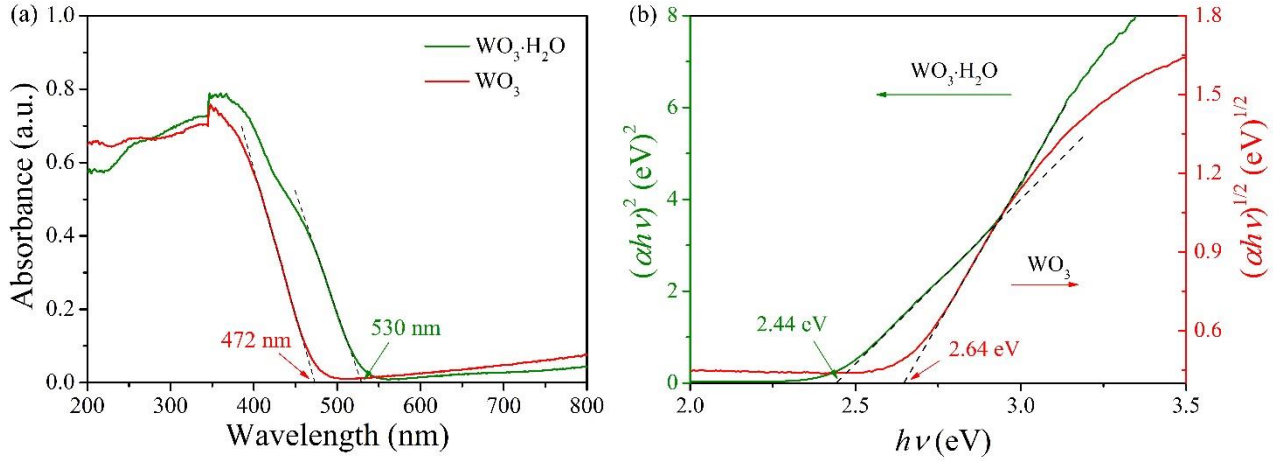

Fig. 7 UV-visible spectra (a) and Tauc's plots (b) of the as-obtained $WO_3 \cdot H_2O$ and WO_3 nanosheets.

Photocatalytic activity evaluation

In general, valence band energy of WO_3 is more positive than the standard redox potential of H_2O/O_2 (1.23 V *vs.* NHE, pH0), suggesting that the photo-generated holes of WO_3 could theoretically oxidize H_2O to produce O_2 [46]. Nevertheless, it is well known that transferring and separation of charge carriers play important roles in the photocatalytic process because only a small percentage of

excited charges, particularly holes, could efficiently take part in O_2-evolution reaction. To investigate the effects of crystal phase and nanostructure on photocatalytic O_2 evolution from water, WO_3 nanosheets were used to compare with $WO_3 \cdot H_2O$ nanosheets and commercial WO_3 powder. In Fig. 8a, the concentration of O_2 evolution from water after 3 h was 69 μmol/L for WO_3 nanosheets, which is 6.3 and 3.6 times higher than that of $WO_3 \cdot H_2O$ nanosheets (11 μmol/L) and commercial WO_3 (19 μmol/L). Meanwhile, it is found that $WO_3 \cdot H_2O$ nanosheets exhibits less O_2-evolving ability than commercial WO_3 powder in spite of the larger photo response range of $WO_3 \cdot H_2O$. This result indicates that the photocatalytic water oxidation of WO_3 nanosheets was significantly enhanced after crystalline transformation by calcination. The stability of photocatalytic water oxidation is presented in Fig. 8b, where WO_3 nanosheets still exhibited considerable stability after 4 recycling, though the photocatalytic performance was to some degree undermined due to deposition of Ag^0 under simulated sunlight illumination.

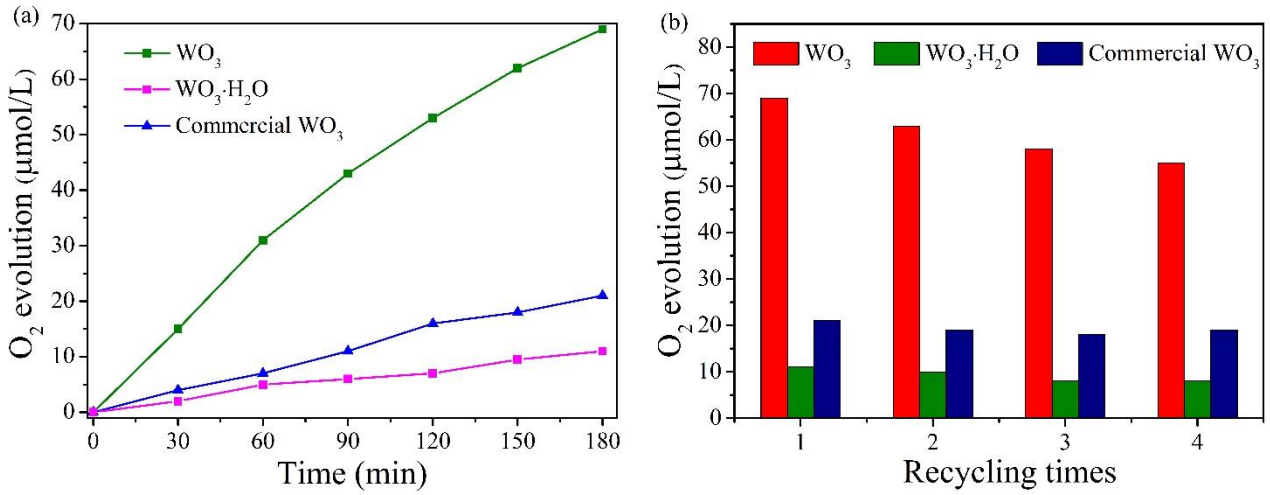

Fig. 8 The photocatalytic O_2 evolution curves of $WO_3 \cdot H_2O$, WO_3 nanosheets, and commercial WO_3.

To further investigate the relationship between crystal transformation and photocatalytic ability, the three samples were further used for oxidation of an organic pollutant, methylene blue (MB). From Fig. 9a, it is seen that WO_3 nanosheets display the best photocatalytic ability compared with $WO_3 \cdot H_2O$ nanosheets and commercial WO_3. The MB degradation rate of WO_3 nanosheets is 4.2 and 6.7 times higer than that of $WO_3 \cdot H_2O$ nanosheets and commcercial WO_3, respectively (Fig. 9b). These results demonstrate that the crystalline transformation from $WO_3 \cdot H_2O$ to WO_3 leads to the

releasing of crystal hydrate, which is beneficial for transferrring photoinduced electrons and holes despite $WO_3 \cdot H_2O$ nanosheets have a better light responsive ability in comparison with WO_3 nanosheets.

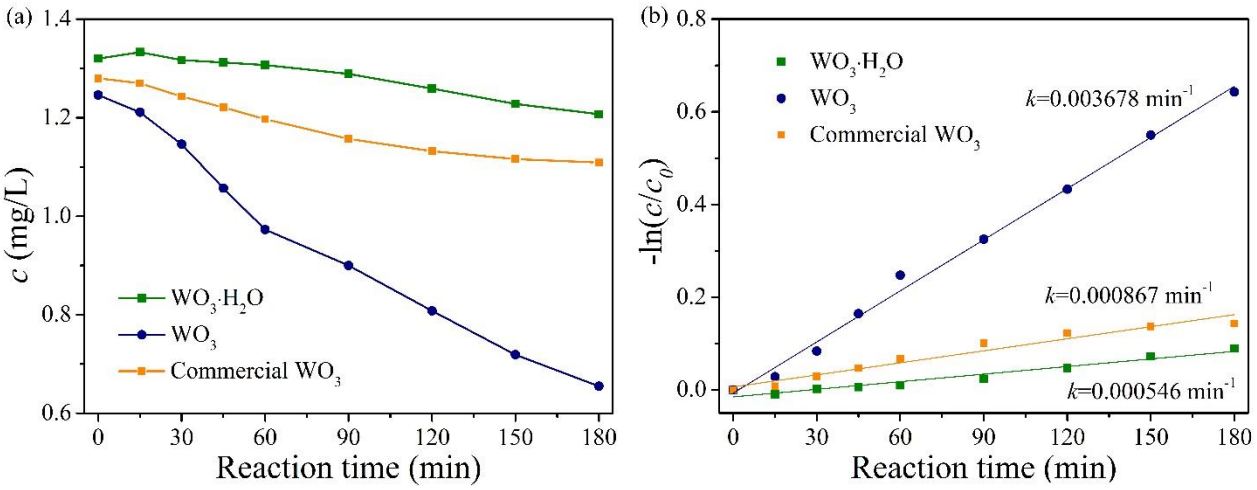

Fig. 9 Photocatalytic activity (a) and reaction kinetics (b) of MB over the as-prepared $WO_3 \cdot H_2O$, WO_3 nanosheets, and commercial WO_3 under simulated sunlight irradiation.

The radical trapping experiments were performed to reveal the active specie during the photocatalytic degradation process by adding tert-butyl alcohol (TBA, hydroxyl radical scavenger), ammonium oxalate (AO, hole scavenger), benzoquinone (BQ, electron scavenger), and nitrogen (N_2, removal of superoxide anion) [47,48]. As shown in Fig. 10, it is clearly found that the scavenging of photo-generated electrons significantly enhances the photocatalytic activity due to the improvement of electron and hole separation. Moreover, the addition of TBA and AO leads to the apparent reduction of photocatalytic activity, which indicates that the dominant active specie is hydroxyl radical. When the photogenerated holes are formed on the surface of WO_3, they react rapidly to produce hydroxyl radical to oxide the organic dye. The TBA has more evident influence in photocatalytic activity, while the superoxide anion removed by N_2 shows a minor effect, which suggests that photoinduced electrons directly work for photocatalytic reaction. These results demonstrate that the hydroxyl radicals deriving from the further oxidation of holes are the domain active species during the photocatalytic degradation.

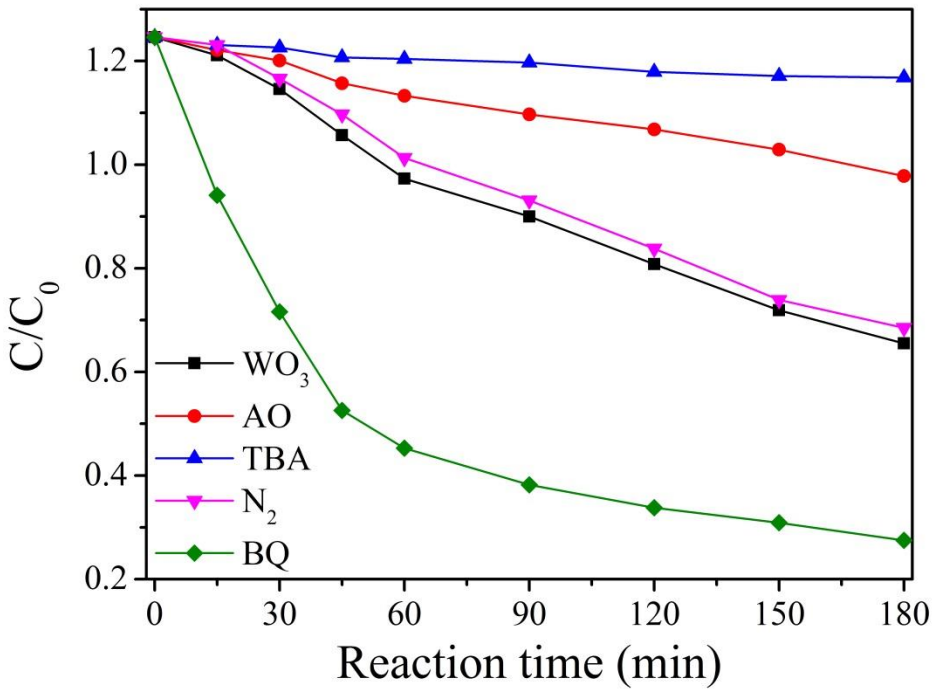

Fig. 10 Decolorization efficiency of MB in the presence of different radical scavengers over WO_3 nanosheets.

N_2 adsorption and desorption isotherms tests have been conducted to obtain the specific surface areas, as shown in Fig. 11. The prepared WO_3•H_2O and WO_3 samples and the commercial WO_3 show similar adsorption isotherms of type IV with a hysteresis loop [49, 50]. The values of the BET specific surface areas of WO_3•H_2O, WO_3, and commercial WO_3 were calculated to be 38, 36, and 22 m^2 g^{-1}, respectively. The as-prepared nanosheet samples have a larger specific area than that of the commercial WO_3 due to the nanoscaled structure and highly exposed surface. Meanwhile, the annealing treatment slightly decreases the surface area of the WO_3 due to the aggregation of nanosheets, which reduces the exposed surface area. In spite of the slightly decreased specific area for the WO_3 sample, the corresponding photocatalytic water oxidation is enhanced in comparison with the WO_3•H_2O and commercial WO_3, which indicates that the improvement of photocatalytic activity results from the crystal transformation accompanying with energy level redistribution.

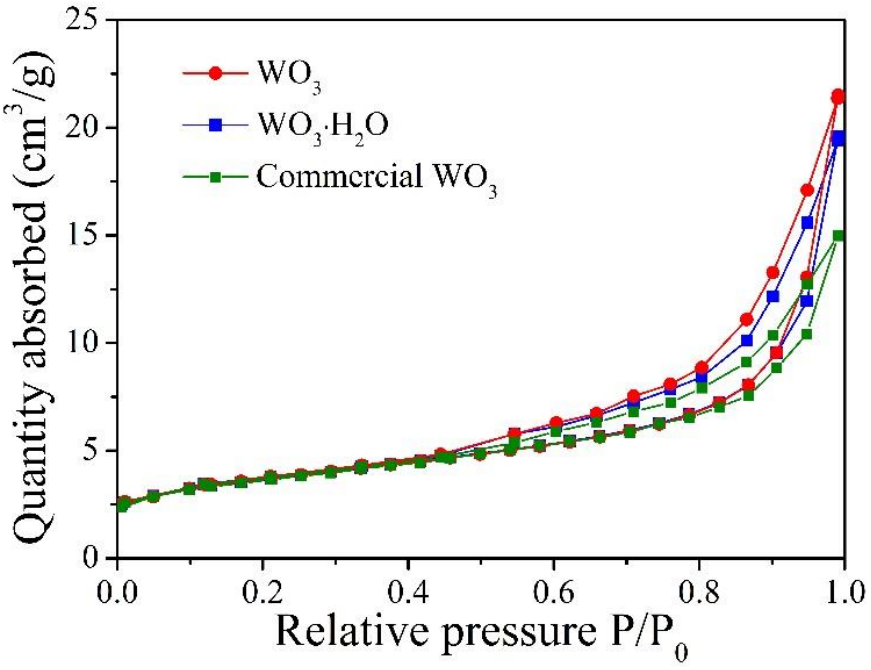

Fig. 11 Nitrogen adsorption-desorption isotherms of the prepare WO_3•H_2O, WO_3, and commercial WO_3.

Photocatalytic mechanism

From the above results, the photocatalytic water oxidation process over $WO_3 \cdot H_2O$ and WO_3 was proposed and displayed in Fig. 12. For the WO_3 nanosheets, the values of conduction band and valence band are located at 0.77 and 3.41 eV *vs. NHE*, pH0, respectively. Nevertheless, the reaction mechanism of photoinduced charge carriers was proposed for the real catalytic reaction in the neutral aqueous solution (pH6.8). The relative positions of CB and VB vs. *NHE*, pH6.8 should be converted through the following equation, $E_{CB,pH}=E_{CB,\ pH0}$ - 0.059*pH*, where $E_{CB,pH}$ is the value of conduction band at specific pH value, $E_{CB,\ pH0}$ is the value of conduction band at pH0 [51, 52]. So the CB and VB values of WO_3 nanosheets at pH6.8 are 0.34 eV and 3.01 eV *vs. NHE*, pH6.8, respectively. In the case of $WO_3 \cdot H_2O$ nanosheets, the conduction band and valence band are located at 0.76 and 3.20 eV, respectively. Meanwhile, the potential of Ag^+/Ag is converted from 0.8 V, pH0 to 0.4 V, pH6.8, respectively. On the other hand, the electrode potentials of H^+/H_2 and O_2/H_2O are situated at - 0.4 and 0.83 V *vs. NHE*, pH=6.8, which implies that $WO_3 \cdot H_2O$ and WO_3 nanosheets could theoretically oxidize water to produce dioxygen but not hydrogen [53]. Nevertheless, the rapid recombination of photoinduced electrons and holes leads to the low evolution of O_2. When the Ag^+ was introduced as

an electron scavenger, the recombination of photoinduced electrons and holes is suppressed. Generally, the electrode potential of $Ag^+/Ag(s)$ is 0.4 V *vs. NHE*, pH=6.8, which is lower than the potential of conduction band of WO_3. Therefore, the photoexcited electrons could easily react with the adsorbed Ag^+ ions, resulting in the efficient O_2-evolution. In contrast, the potential of the conduction band of $WO_3 \cdot H_2O$ is lower than that of $Ag^+/Ag(s)$, which could not trigger the reduction reaction of Ag^+. Consequently, the excited electrons could recombine with the holes at the valence band, leading to low efficiency of photocatalytic water oxidation. As discussed above, the crystalline transformation ascribed to calcination not only realizes the removal of crystal hydrate, but also leads to the realignment of energy level, which allows more photogenerated electrons and holes to participate in the reduction and oxidation reactions for oxidizing water molecules and pollutants.

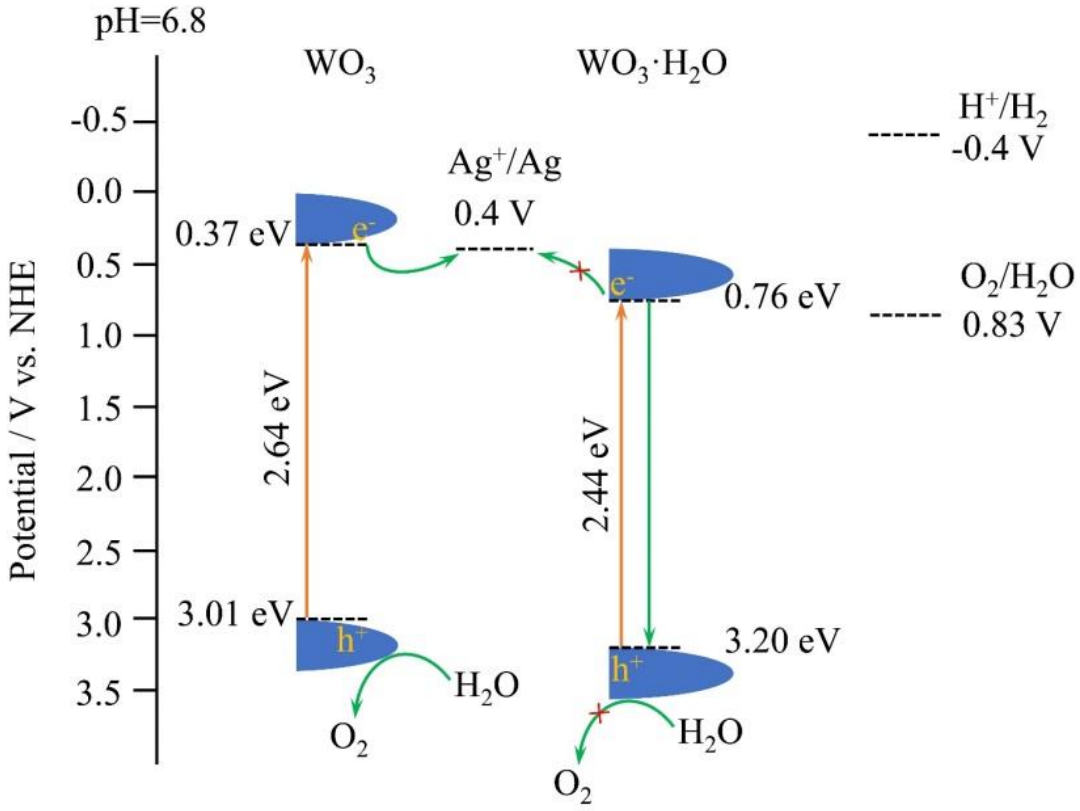

Fig. 12 The illustrated scheme of photocatalytic water oxidation over the $WO_3 \cdot H_2O$ and WO_3 nanosheets in the present of Ag^+.

Conclusions

In this work, we successfully fabricated 2D WO_3 nanosheets by a facile hydrothermal and calcination method for photocatalytic O_2 evolution from water. The WO_3 nanosheets show uniform morphology

with an average diameter of 2-3 μm and display an enhanced O_2 production, which is 6.3 and 3.6 times higher than that of the $WO_3 \cdot H_2O$ nanosheets and commercial WO_3. $WO_3 \cdot H_2O$ has better visible light response than WO_3 nanosheets, while the photocatalytic water oxidation activity is less due to the disadvantageous energy band alignment in the present of Ag^+ as an electron scavenger under neutral condition. It is demonstrated that the releasing of water molecules in the crystal phase of tungstic acid results in transformation of the crystal phase from orthorhombic $WO_3 \cdot H_2O$ to monoclinic WO_3, significantly enhancing the photocatalytic water oxidation activity because the shift-up of the conduction band of WO_3 matches well with the electrode potential of $Ag^+/Ag(s)$, leading to the efficient separation of photoinduced electrons and holes in pure WO_3 nanosheets.

Acknowledgements

This work was financially supported by the National Natural Science Foundation of China (21501138), the Natural Science Foundation of Hubei Province (2015CFB177), and the Science Research Foundation of Wuhan Institute of Technology (237822).

Notes and references

[1] T. Hisatomi, J. Kubota, K. Domen, Recent advances in semiconductors for photocatalytic and photoelectrochemical water splitting, Chem. Soc. Rev. 43 (2014) 7520-7535.

[2] D. Fabian, S. Hu, N. Singh, F. Houle, T. Hisatomi, K. Domen, F. Osterloh, S. Ardo, Particle suspension reactors and materials for solar-driven water splitting, Energy Environ. Sci. 8 (2015) 2825-2850.

[3] Y. Yan, B. Xia, B. Zhao, X. Wang, A review on noble-metal-free bifunctional heterogeneous catalysts for overall electrochemical water splitting, J. Mater. Chem. A 4 (2016) 17587-17603.

[4] Y. Li, Y. Li, B. Sa, R. Ahuja, Review of two-dimensional materials for photocatalytic water splitting from a theoretical perspective, Catal. Sci. Technol. 7 (2017) 545-559.

[5] S. Kment, F. Riboni, S. Pausova, L. Wang, L. Wang, H. Han, Z. Hubicka, J. Krysa, P. Schnuki, R. Zboril, Photoanodes based on TiO_2 and α-Fe_2O_3 for solar water splitting-superior role of 1D nanoarchitectures and of combined heterostructures, Chem. Soc. Rev. 46 (2017) 3716-3769.

[6] A. Laursen, S. Kegnas, S. Dahl, I. Chorkendorff, Molybdenum sulfides-efficient and viable materials for electro- and photoelectrocatalytic hydrogen evolution, Energy Environ. Sci. 5 (2012) 5577-5591.

[7] K. Zhang, W. Kim, M. Ma, X. Shi, J. Park, Tuning the charge transfer route by p-n junction catalysts embedded with CdS nanorods for simultaneous efficient hydrogen and oxygen evolution, J. Mater. Chem. A 3 (2015) 4803-4810.

[8] J. Liu, Y. Li, J. Ke, S. Wang, L. Wang, H. Xiao, Black NiO-TiO_2 nanorods for solar photocatalysis: recognition of electronic structure and reaction mechanism, Appl. Catal. B: Environ. 224 (2018) 705-714.

[9] P. Sennu, H. Park, K. Park, V. Aravindan, K. Nahm, Y. Lee, Formation of $NiCo_2O_4$ rods over Co_3O_4 nanosheets as efficient catalyst for Li-O_2 batteries and water splitting, J. Catal. 349 (2017) 175-182.

[10] J. Liu, J. Ke, D. Li, H. Sun, P. Liang, X. Duan, W. Tian, M. Tade, S. Liu, S. Wang, Oxygen vacancies in shape controlled Cu_2O/reduced graphene oxide/In_2O_3 hybrid for promoted photocatalytic water oxidation and degradation of environmental pollutants, ACS Appl. Mater. Interfaces 9 (2017) 11678-11688.

[11] T. Jin, P. Diao, Q. Wu, D. Xu, D. Hu, Y. Xie and M. Zhang, WO_3 nanoneedles/α-Fe_2O_3/cobalt phosphate composite photoanode for efficient photoelectrochemical water splitting, Appl. Catal. B: Environ. 148-149 (2014) 304-310.

[12] J. Xiao, H. Huang, Q. Huang, X. Li, X. Hou, L. Zhao, R. Ma, H. Chen, Y. Li, Remarkable improvement of the turn-on characteristics of a Fe_2O_3 photoanode for photoelectrochemical water splitting with coating a FeCoW oxy-hydroxide gel, Appl. Catal. B: Environ. 212 (2017) 89-96.

[13] J. Ke, J. Liu, H. Sun, H. Zhang, X. Duan, P. Liang, X. Li, M. Tade, S. Liu, S. Wang, Facile assembly of $Bi_2O_3/Bi_2S_3/MoS_2$ n-p heterojunction with layered n-Bi_2O_3 and p-MoS_2 for enhanced photocatalytic water oxidation and pollutant degradation, Appl. Catal. B: Environ. 200 (2017) 47-55.

[14] X. Chen, S. Shen, L. Guo, S. Mao, Semiconductor-based photocatalytic hydrogen generation, Chem. Rev. 110 (2010) 6503-6570.

[15] S. Kalanur, Y. Hwang, S. Chae, O. Joo, Facile growth of aligned WO_3 nanorods on FTO substrate for enhanced photoanodic water oxidation activity, J. Mater. Chem. A 1 (2013) 3479-3488.

[16] H. He, S. Berglund, P. Xiao, W. Chemelewski, Y. Zhang, C. Mullins, Nanostructured Bi_2S_3/WO_3 heterojunction films exhibiting enhanced photoelectrochemical performance, J. Mater. Chem. A 1 (2013) 12826-12834.

[17] S. Pilli, R. Janarthanan, T. Deutsch, T. Furtak, L. Brown, J. Turner and A. Herring, Efficient photoelectrochemical water oxidation over cobalt-phosphate (Co-Pi) catalyst modified $BiVO_4$/1D-WO_3 heterojunction electrodes, Phys.Chem. Chem. Phys. 15 (2013) 14723-14728.

[18] H. Suzuki, S. Nitta, O. Tomita, M. Higashi, R. Abe, Highly dispersed RuO_2 hydrates prepared via simple adsorption as efficient cocatalysts for visible-light-driven Z-scheme water splitting with an IO_3^-/I^- redox mediator, ACS Catal. 7 (2017) 4336-4343.

[19] D. Martin, P. Reardon, S. Moniz, J. Tang, Visible light-driven pure water splitting by a nature-inspired organic semiconductor-based system, J. Am. Chem. Soc. 136 (2014) 12568-12571.

[20] H. Suzuki, O. Tomita, M. Higashi, R. Abe, Tungstic acids H_2WO_4 and H_4WO_5 as stable photocatalysts for water oxidation under visible light, J. Mater. Chem. A 5 (2017) 10280-10288.

[21] D. Chen, J. Ye, Hierarchical WO_3 hollow shells: dendrite, sphere, dumbbell, and their photocatalytic properties, Adv. Funct. Mater. 18 (2008) 1922-1928.

[22] J. Cao, B. Luo, H. Lin, B. Xu, S. Chen, Thermodecomposition synthesis of WO_3/H_2WO_4 heterostructures with enhanced visible light photocatalytic properties, Appl. Catal. B: Environ. 111-112 (2012) 288-296.

[23] D. Chen, L. Gao, A. Yasumori, K. Kuroda, Y. Sugahara, Size- and shape-controlled conversion of Tungstate-based inorganic-organic hybrid belts to WO_3 nanoplates with high specific surface areas, Small 4 (2008) 1813-1822.

[24] J. Guo, Y. Li, S. Zhu, Z. Chen, Q. Liu, D. Zhang, W. Moon, D. Song, Synthesis of WO_3@Graphene composite for enhanced photocatalytic oxygen evolution from water, RSC Adv. 2 (2012) 1356-1363.

[25] M. Xu, W. Zeng, F. Yang, L. Chen, Controllability of assemblage from $WO_3 \cdot H_2O$ nanoplates to nanoflowers with the assistance of oxalic acid, J. Mater. Sci: Mater. Electron. 26 (2015) 6676-6682.

[26] L. Li, J. Zhao, Y. Wang, Y. Li, D. Ma, Y. Zhao, S. Hou, X. Hao, Oxalic acid mediated synthesis of $WO_3 \cdot H_2O$ nanoplates and self-assembled nanoflowers under mild conditions, J. Solid State Chem. 184 (2011) 1661-1665.

[27] J. Zhang, P. Zhang, T. Wang, J. Gong, Monoclinic WO_3 nanomultilayers with preferentially exposed (002) facets for photoelectrochemical water splitting, Nano Energy 11 (2015) 189-195.

[28] N. Zhang, C. Chen, Z. Mei, X. Liu, X. Qu, Y. Li, S. Li, W. Qi, Y. Zhang, J. Ye, V. Roy, R. Ma, Monoclinic tungsten oxide with {100} facet orientation and tuned electronic band structure for enhanced photocatalytic oxidations, ACS Appl. Mater. Interfaces 8 (2016) 10367-10374.

[29] S. Bai, K. Zhang, R. Luo, D. Li, A. Chen, C. Liu, Low-temperature hydrothermal synthesis of WO_3 nanorods and their sensing properties for NO_2, J. Mater. Chem. 22 (2012) 12643-12650.

[30] Z. Wang, S. Zhou, L. Wu, Preparation of rectangular $WO_3 \cdot H_2O$ nanotubes under mild conditions, Adv. Funct. Mater. 17 (2007) 1790-1794.

[31] L. Liang, J. Zhang, Y. Zhou, J. Xie, X. Zhang, M. Guan, B. Pan, Y. Xie, High performance flexible electrochromic device based on facile semiconductor-to-metal transition realized by $WO_3 \cdot 2H_2O$ ultrathin nanosheets, Sci. Rep. 3 (2013) 1936.

[32] Y. Oaki, H. Imai, Room-temperature aqueous synthesis of highly luminescent $BaWO_4$-Polymer nanohybrids and their spontaneous conversion to hexagonal WO_3 nanosheets, Adv. Mater. 18 (2006) 1807-1811.

[33] G. Xi, B. Yue, J. Cao, J. Ye, Fe_3O_4/WO_3 hierarchical core-shell structure: high-performance and recyclable visible-light photocatalysis, Chem. Eur. J. 17 (2011) 5145-5154.

[34] T. Gao, B. Jelle, Visible-light-driven photochromism of hexagonal sodium tungsten bronze nanorods, J. Phys. Chem. C 117 (2013) 13753-13761.

[35] J. Ding, Q. Liu, Z. Zhang, X. Liu, J. Zhao, S. Cheng, B. Zong, W. Dai, Carbon nitride nanosheets decorated with WO_3 nanorods: ultrasonic-assisted facile synthesis and catalytic application in the green manufacture of dialdehydes, Appl. Catal. B: Environ. 165 (2015) 511.

[36] X. Chen, Y. Zhou, Q. Liu, Z. Li, J. Liu, Z. Zou, Ultrathin, Single-crystal WO_3 nanosheets by two-dimensional oriented attachment toward enhanced photocatalystic reduction of CO_2 into hydrocarbon fuels under visible light, ACS Appl. Mater. Interfaces 4 (2012) 3372-3377.

[37] X. Li, W. Wang, D. Jiang, S. Sun, L. Zhang, X. Sun, Efficient solar-driven nitrogen fixation over Carbon-Tungstic-acid hybrids, Chem. Eur. J. 22 (2016) 13819-13822.

[38] J. Dai, W. Zhong, W. Yi, M. Liu, L. Mao, Q. Xu, D. Yin, Bifunctional H_2WO_4/TS-1 catalysts for direct conversion of cyclohexane to adipic acid: active sites and reaction step, Appl. Catal. B: Environ. 192 (2016) 325-341.

[39] Y. He, Y. Zhao, Near-infrared laser-induced photothermal coloration in $WO_3 \cdot H_2O$ nanoflakes, J. Phys. Chem. C 112 (2008) 61-68.

[40] B. Weng, J. Wu, N, Zhang, Y. Xu, Observing the role of graphene in boosting the two-electron reduction of oxygen in graphene-WO_3 nanorod photocatalysts, Langmuir 30 (2014) 5574-5584.

[41] Y. Liu, J. Li, W. Li, Y. Yang, Y. Li, Q. Chen, Enhancement of the photoelectrochemical performance of WO_3 vertical arrays film for solar water splitting by Gadolinium doping, J. Phys. Chem. C 119 (2015) 14834-14842.

[42] J. Cao, B. Luo, H. Lin, S. Chen, Synthesis, characterization and photocatalytic activity of $AgBr/H_2WO_4$ composite photocatalyst, J. Mol. Catal. A: Chem. 344 (2011) 138-144.

[43] Z. Gao, S. Xie, B. Zhang, X. Qiu, F. Chen, Ultrathin Mg-Al layered double hydroxide prepared by ionothermal synthesis in a deep eutectic solvent for highly effective boron removal, Chem. Eng. J, 319 (2017) 108-118.

[44] Y. Xu, Z, Zhang, W. Zhang, Inlay of $Bi_2O_2CO_3$ nanoparticles onto Bi_2WO_6 nanosheets to build heterostructured photocatalysts, Dalton Trans. 43 (2014) 3660-3668.

[45] Y. Wei, G. Cheng, J. Xiong, F. Xu, R. Chen, Positive $Ni(HCO_3)_2$ as a novel cocatalyst for boosting the photocatalytic hydrogen evolution capability of mesoporous TiO_2 nanocrystals, ACS Sustainable Chem. Eng. 5 (2017) 5027-5038.

[46] Z. Hu, M. Xu, Z. Shen, J. Yu, A nanostructured chromium (III) oxide/tungsten (VI) oxide p-n junction photoanode toward enhanced efficiency for water oxidation, J. Mater. Chem. A 3 (2015) 14046-14053.

[47] H. Jiaoa, X. Yua, Z. Liu, P. Kuang, Y. Zhang, One-pot synthesis of heterostructured Bi_2S_3/BiOBr microspheres with highly efficient visible light photocatalytic performance, RSC Adv. 5 (2015) 16239-16249.

[48] W. Raza, S. Faisal, M. Owais, D. Bahnemann, M. Muneer, Facile fabrication of highly efficient modified ZnO photocatalyst with enhanced photocatalytic, antibacterial and anticancer activity, RSC Adv. 6 (2016) 78335-78350.

[49] S. Luo, J. Ke, M. Yuan, Q. Zhang, P. Xie, L. Deng, S. Wang, $CuInS_2$ quantum dots embedded in Bi_2WO_6 nanoflowers for enhanced visible light photocatalytic removal of contaminants, Appl. Catal. B: Environ. 221 (2018) 215-222.

[50] J. Liu, X. Li, R. Li, Q. Zhao, J. Ke, H. Xiao, L. Wang, S. Liu, M. Tadé, S. Wang, Facile synthesis of tube-shaped Mn-Ni-Ti solid solution and preferable Langmuir-Hinshelwood mechanism for selective catalytic reduction of NO_x by NH_3, Appl. Catal. A Gen. 549 (2018) 289-301.

[51] Y. Xu, M. Schoonen, The absolute energy positions of conduction and valence bands of selected semiconducting minerals, Am. Mineral. 85 (2000) 543-556.

[52] B. Xie, H. Zhang, P. Cai, R. Qiu, Y. Xiong, Simultaneous photocatalytic reduction of Cr(VI) and oxidation of phenol over monoclinic $BiVO_4$ under visible light irradiation, Chemosphere 63 (2006) 956-963.

[53] K. Fuku, K. Sayama, Efficient oxidative hydrogen peroxide production and accumulation in photoelectrochemical water splitting using a tungsten trioxide/bismuth vanadate photoanode, Chem. Commun. 52 (2016) 5406-5409.